

Origin of deep ocean microseisms by using teleseismic body waves

Matthieu Landès, Fabien Hubans, Nikolai M. Shapiro, Anne Paul, Michel Campillo

▶ **To cite this version:**

Matthieu Landès, Fabien Hubans, Nikolai M. Shapiro, Anne Paul, Michel Campillo. Origin of deep ocean microseisms by using teleseismic body waves. Journal of Geophysical Research, 2010, 115, pp.05302. 10.1029/2009JB006918 . insu-00565200

HAL Id: insu-00565200
https://insu.hal.science/insu-00565200

Submitted on 6 Aug 2020

HAL is a multi-disciplinary open access archive for the deposit and dissemination of scientific research documents, whether they are published or not. The documents may come from teaching and research institutions in France or abroad, or from public or private research centers.

L'archive ouverte pluridisciplinaire **HAL**, est destinée au dépôt et à la diffusion de documents scientifiques de niveau recherche, publiés ou non, émanant des établissements d'enseignement et de recherche français ou étrangers, des laboratoires publics ou privés.

JOURNAL OF GEOPHYSICAL RESEARCH, VOL. 115, B05302, doi:10.1029/2009JB006918, 2010

Click Here for Full Article

Origin of deep ocean microseisms by using teleseismic body waves

Matthieu Landès,[1] Fabien Hubans,[2] Nikolai M. Shapiro,[1] Anne Paul,[2] and Michel Campillo[2]

Received 2 September 2009; revised 1 December 2009; accepted 17 December 2009; published 5 May 2010.

[1] Recent studies of oceanic microseisms have concentrated on fundamental mode surface waves. Extraction of fundamental mode Rayleigh and Love wave Green functions from station-station correlations of ambient seismic noise has recently been demonstrated to be a very powerful tool for imaging of the Earth's crust and uppermost mantle. In this study we concentrate on energetic arrivals in two frequency bands around the primary (14 s) and the secondary (7 s) microseismic peaks that appear at near-zero times in noise cross correlations. Thanks to a polarization analysis of data from the Eastern Turkey Seismic Experiment network, we identify this "near-zero time" signal as an upcoming *P* wave in the secondary microseismic frequency band (5–10 s). In a second step, analyzing noise cross correlations from three different arrays (in Yellowstone, in Turkey, and in Kyrgyzstan), we determine the origin of these signals by means of beam-forming analysis and its projection on the Earth. Our results show that in the 0.1–0.3 Hz frequency band, the energetic "near-zero" time arrivals in seismic noise cross correlations are mainly formed by teleseismic *P*, *PP*, and *PKP* waves. Generation of this ambient body waves in the secondary microseismic band presents a marked seasonal behavior with sources located in southern and northern oceans during summer and winter, respectively. Moreover, body wave array analysis is accurate enough to confirm that significant amount of the microseism energy is generated far from the coast in deep oceans.

Citation: Landès, M., F. Hubans, N. M. Shapiro, A. Paul, and M. Campillo (2010), Origin of deep ocean microseisms by using teleseismic body waves, *J. Geophys. Res.*, *115*, B05302, doi:10.1029/2009JB006918.

1. Introduction

[2] Recent years witnessed a strong interest in studying background seismic noise. One of the reasons for this interest is the possibility to extract deterministic Green functions from correlations of a random wavefield that can be proved mathematically with different approaches [e.g., *Lobkis and Weaver*, 2001; *Snieder*, 2004; *Gouédard et al.*, 2008] and that has been demonstrated in acoustic laboratory experiments [e.g., *Lobkis and Weaver*, 2001; *Derode et al.*, 2003]. Application of this principle to large amount of continuous digital seismic records provided by modern networks provides us with new approaches for seismic tomography [e.g., *Shapiro and Campillo*, 2004; *Shapiro et al.*, 2005; *Sabra et al.*, 2005; *Yang et al.*, 2007; *Stehly et al.*, 2009] and monitoring [e.g., *Sens-Schönfelder and Wegler*, 2006; *Brenguier et al.*, 2008b, 2008a]. Detailed analysis of high-quality continuous records also allows us to better understand the origin of the ambient seismic noise and its relation to oceanic and atmospheric processes. New methods of noise-based seismic imaging and monitoring are based on a principle that the Green function between two points can be extracted by correlating a random wavefield recorded by receivers located in these points. In other words, one of the two receivers can be considered as a virtual source recorded by the second receiver. This principle is especially attractive when applied in context of random wavefield recorded by a network of numerous recorders. In this case, by computing all possible interstation cross correlations it becomes possible to place virtual sources at every receiver location and to have their records by the whole network resulting in a very dense path coverage. The deterministic waveforms (Green functions) extracted from the cross correlations can be used then to measure and to invert travel times with different methods developed in context of earthquake or explosion based seismology.

[3] The noise-based Green function reconstruction implies, however, some strong hypothesis about the noise modal composition. A perfect reconstruction can be achieved for an ideally random and equipartitioned wavefield [*Lobkis and Weaver*, 2001; *Sánchez-Sesma and Campillo*, 2006]. In a case of seismic noise it would imply that its sources should be distributed randomly and homogeneously in volume. This is obviously not the case for the real ambient seismic noise within the Earth. First, most of its sources are located on the surface resulting in stronger presence of fundamental mode surface waves and their relatively easy reconstruction from interstation cross correlations. For the same reasons, extracting body wave Green functions from noise cross correlations

[1]Institut de Physique du Globe de Paris, CNRS, Paris, France.
[2]Laboratoire de Géophysique Interne et Tectonophysique, Université Joseph Fourier, CNRS, Grenoble, France.

Copyright 2010 by the American Geophysical Union.
0148-0227/10/2009JB006918

remains challenging. Second, the distribution of noise sources is not perfectly random and homogeneous. Background seismic oscillations are mostly generated by the forcing from oceanic gravity and infragravity waves. The interaction between these oceanic waves and the solid Earth is governed by a complex nonlinear mechanism [e.g., *Longuet-Higgins*, 1950] and, as a result, the noise excitation depends on many factors such as the intensity of the oceanic waves but also the intensity of their interferences as well as the seafloor topography [e.g., *Kedar et al.*, 2008]. Overall, the generation of seismic noise is strongly modulated by strong oceanic storms and therefore, has a clear seasonal and nonrandom pattern.

[4] Distribution of noise sources homogenizes when considered over long times (more than 1 year). The homogenization and randomization of the noise wavefield is also enhanced by the scattering of the seismic waves on the small-scale heterogeneity within the Earth. Also, because of the stationary phase principle, a cross correlation of the noise recorded by two receivers is dominated by contribution from sources located in vicinity of the line connecting these receivers. Therefore, even without a perfectly homogeneous distribution, a presence of sufficient amount of favorably located noise sources results in relatively high-quality reconstruction of fundamental mode surface waves. As a consequence, reconstructing surface waves from correlations of seismic noise and measuring their dispersion curves works rather well. However, further improving the accuracy of the noise based measurements needed to develop new high-resolution imaging and monitoring methods requires better understanding of the noise modal content and its evolution in space and time. Taking into account realistic distribution of noise sources is also necessary to be able to apply waveform inversion approaches to the noise correlations.

[5] Seismic noise spectra contains two prominent peaks at 0.05–0.1 and 0.1–0.3 Hz called primary and secondary microseisms, respectively. The primary microseism originates from direct forcing of strong oceanic waves while the secondary microseism which is characterized by stronger amplitudes is produced at double frequency by a nonlinear interaction of these waves as suggested by *Longuet-Higgins* [1950]. Both microseismic peaks are dominated by fundamental mode surface waves. It is currently debated whether the surface wave component of microseisms is generated primarily along coastlines [e.g., *Friedrich et al.*, 1998; *Bromirski and Duennebier*, 2002; *Essen et al.*, 2003; *Schulte-Pelkum et al.*, 2004; *Rhie and Romanowicz*, 2006; *Yang and Ritzwoller*, 2008] or if it is also generated in deep-sea areas [*Cessaro*, 1994; *Stehly et al.*, 2006; *Chevrot et al.*, 2007; *Kedar et al.*, 2008]. At the same time, body waves were detected in the secondary microseismic band using dense seismic arrays [e.g., *Backus et al.*, 1964; *Toksöz and Lacoss*, 1968; *Seriff et al.*, 1965; *Iyer and Healy*, 1972; *Koper and de Foy*, 2008; *Gerstoft et al.*, 2008] and can be often associated with specific storms [e.g., *Gerstoft et al.*, 2006]. Inhomogeneous distribution of noise sources is clearly revealed by the asymmetry of noise cross correlations observed in both primary and secondary microseismic bands [e.g., *Stehly et al.*, 2006; *Yang and Ritzwoller*, 2008]. According to Longuet-Higgins' theory, the generation of secondary microseisms is associated with the nonlinear interaction of swells propagating in opposite directions. Such a configuration can be encountered in the coastal region where incident and reflected waves are likely present. This is the case that is considered as prominent by the seismologists based on the observations of the radiation by individual storms [e.g., *Bromirski and Duennebier*, 2002; *Gerstoft and Tanimoto*, 2007; *Bromirski*, 2009]. Although there is little doubt that a part of the ambient noise is related with the interaction of oceanic waves with the coast, it is not the only situation where waves propagating in opposite directions are encountered. *Kedar et al.* [2008] used a wave action model to implement Longuet-Higgins theory and found that particular regions in the deep oceans are potential sources of secondary microseism excitation. This is related to specific conditions of meteorological forcing associated with resonances of the water column. Their results indicate that secondary microseisms can be generated in specific deep-water areas with one example in the Atlantic ocean south of Greenland.

[6] To investigate the location of the sources of the background noise, we use seismological data averaged over long time series. The Rayleigh wave part of the noise in the secondary microseism period band rapidly attenuates with distance. It is therefore difficult to assess the locations of sources when the signal is dominated by the closest source, often the closest coast, that hides the remote sources. To overcome this difficulty, we use *P* wave at teleseismic distances recorded in continental environments.

[7] We compute noise cross correlations for three seismic arrays located within continents in the Northern hemisphere. During summer months, when most of strong storms are located in the Southern hemisphere, the observed noise cross correlations are dominated by arrivals at near-zero times. Polarization analysis clearly indicates that these arrivals are composed of teleseismic *P* waves. We then use a beam-forming analysis to determine precisely back azimuths and slowness corresponding to these arrivals and to back project them to the regions where the energy was generated based on ray tracing in a global spherically symmetric Earth model.

1.1. Polarization Analysis to Detect Teleseismic *P* Waves in Noise Cross Correlations

[8] In this section, we use the data of the Eastern Turkey Seismic Experiment (ETSE) that operated a temporary network of 20 broadband stations between October 1999 and August 2001 (Figure 1) [*Sandvol et al.*, 2003].

1.1.1. Data Preprocessing

[9] Polarization analysis of noise cross correlations requires preserving the amplitude ratio between components. Therefore, standard processing for the computation of noise cross correlations such as one-bit normalization and spectral whitening, cannot be applied. Instead, data are corrected for instrumental responses, resampled to 1 Hz and filtered between 0.01 and 0.3 Hz. A water level of 4 times the standard deviation of each record is used to decrease the amplitude effect of earthquakes on cross correlations. Furthermore, for each station and each component, only daily records with mean energy smaller than the whole experiment mean energy are used for the polarization analysis.

1.1.2. Noise Cross Correlations

[10] Figures 2 and 3 show cross correlations between vertical noise records (ZZ) plotted with respect to distance between stations for two different seasons and two frequency bands which correspond to primary and secondary microseismic peaks (0.05–0.1 Hz and 0.1–0.3 Hz). A propagating

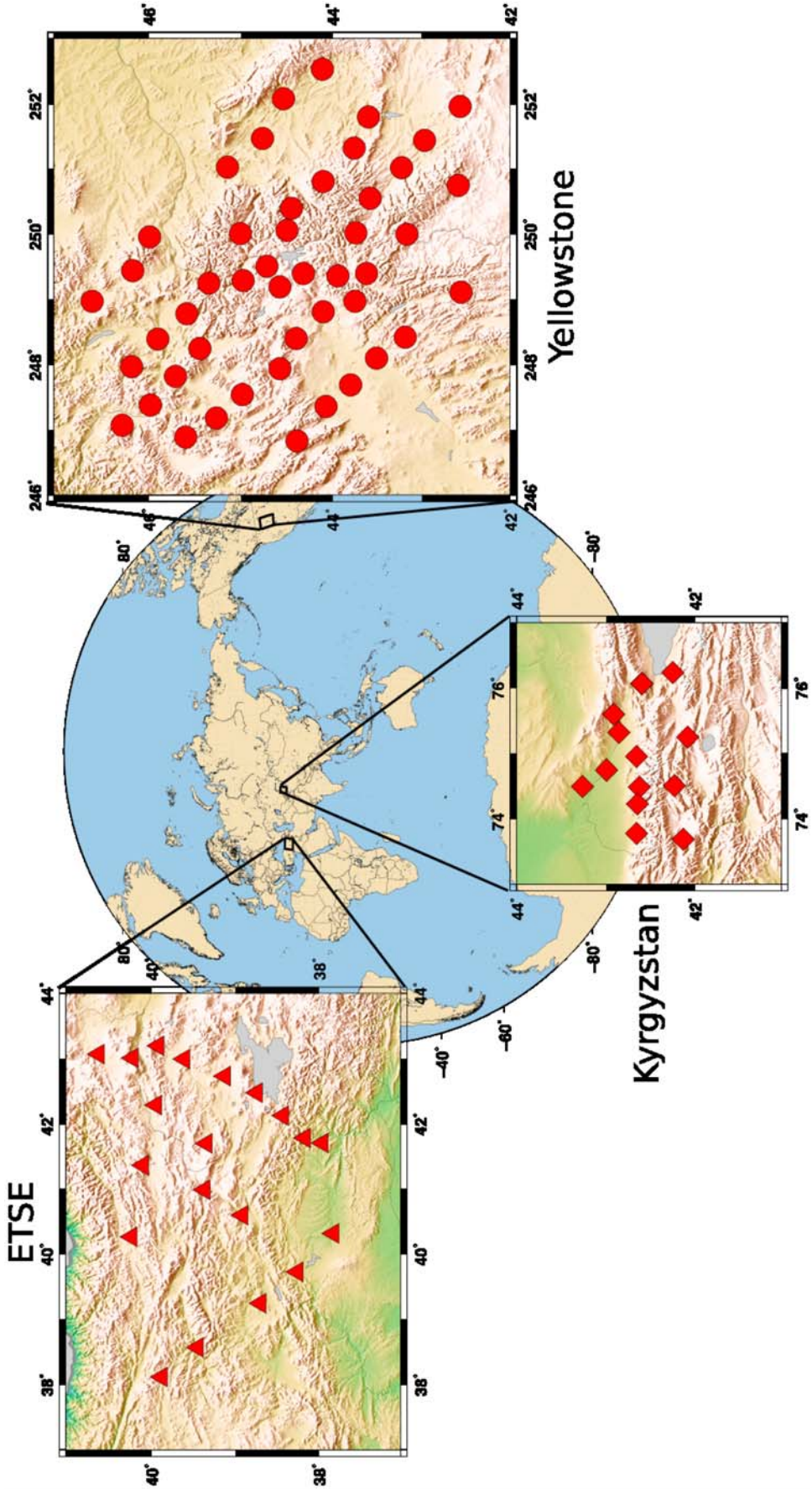


Figure 1. Maps of ETSE, Yellowstone, and Kyrgyzstan networks.

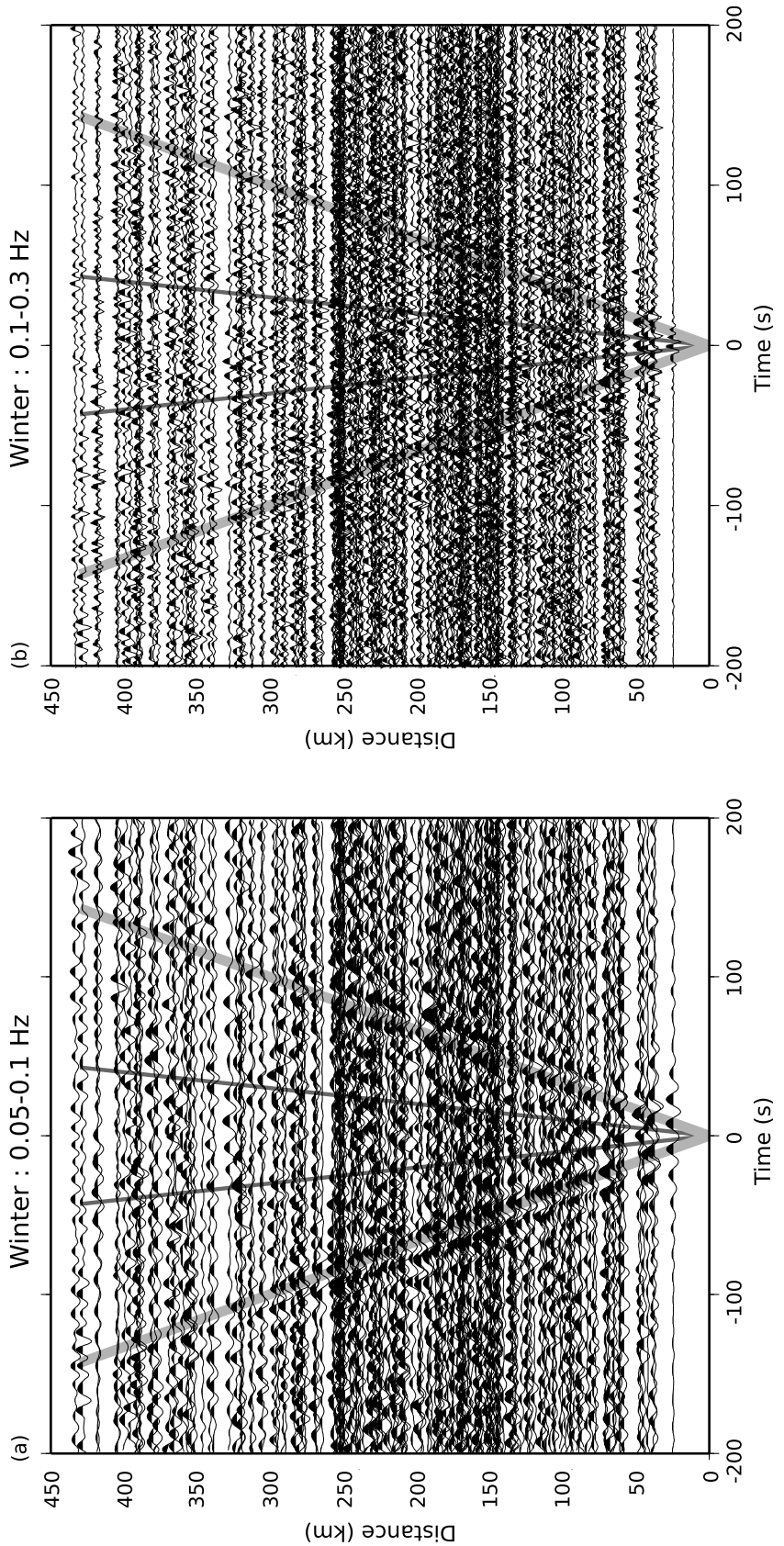


Figure 2. Cross correlations of vertical component records between stations of the ETSE network stacked for months between September and March (winter) for years 1999, 2000, and 2001 plotted as function of the distance between the pair of stations in the (a) 0.05–0.1 Hz and (b) 0.1–0.3 Hz frequency bands.

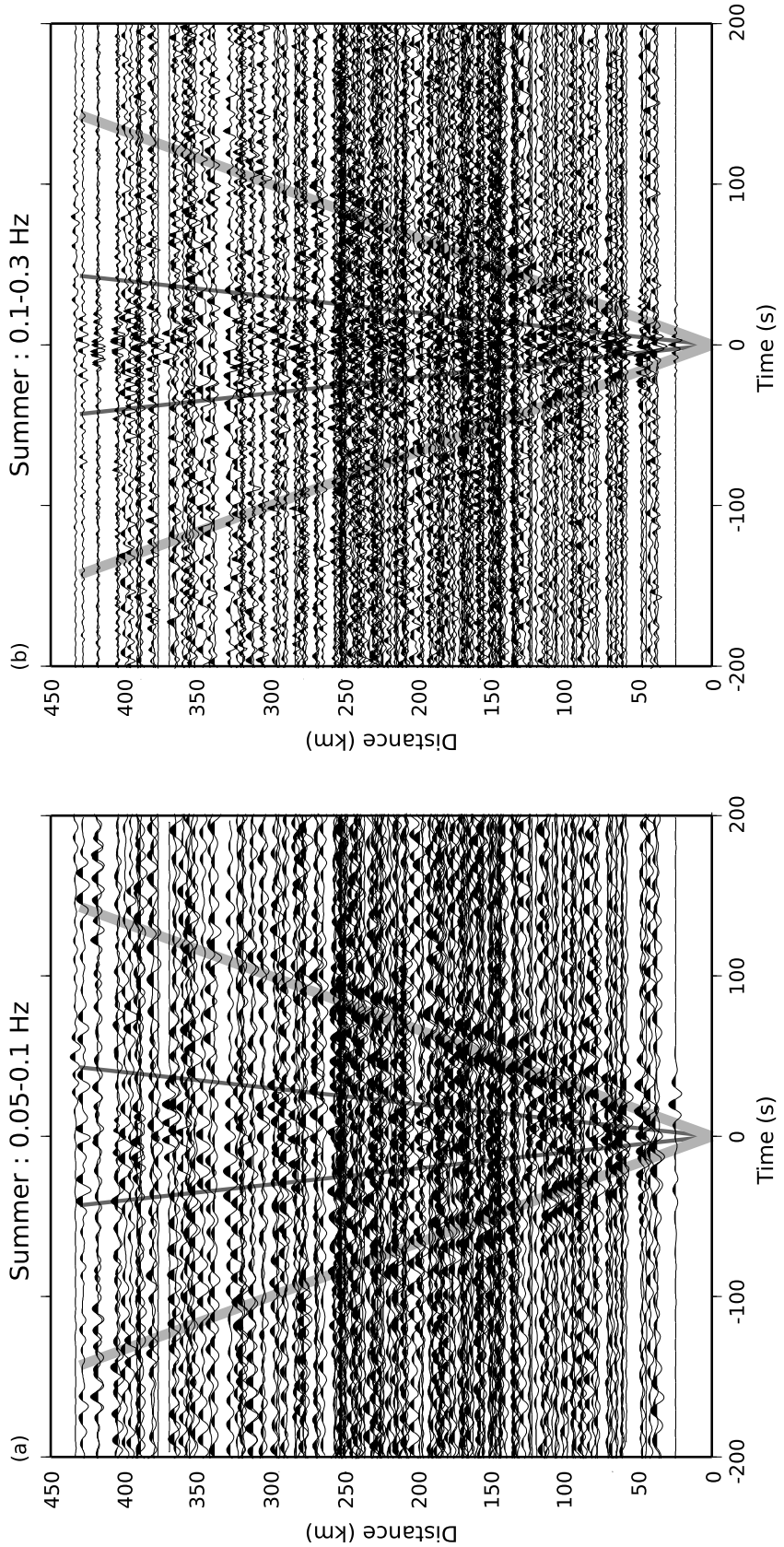


Figure 3. Cross correlations of vertical component records between stations of the ETSE network stacked for months between April and August (summer) for years 1999, 2000, and 2001 plotted as function of the distance between the pair of stations in the (a) 0.05–0.1 Hz and (b) 0.1–0.3 Hz frequency bands.

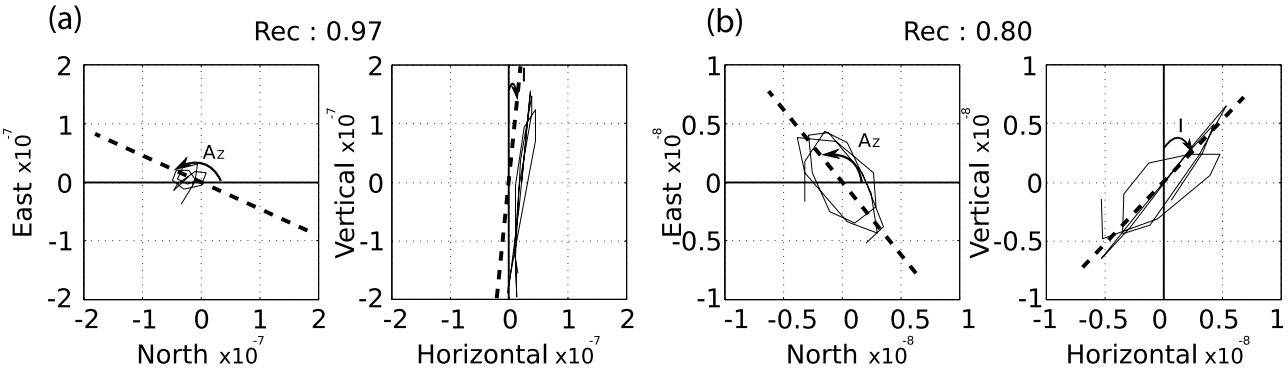


Figure 4. Particle motion for two station pairs from noise correlations in the [−10 s; +10 s] time window for the band 0.1–0.2 Hz. (a) Cross correlations between KARS and KOTK (distance 391 km) for 30 October 1999; (b) cross correlations between KARS and ILIC (distance 404 km) for 23 March 2000. Rec is the rectilinearity coefficient defined by equation (1). Dashed lines show the incidence angle and the azimuth measured from the covariance method.

wave with apparent velocity close to 3 km/s (thick gray lines) is observed at negative and positive times. This time-symmetrical signal which is stronger in the 0.05–0.1 Hz bandpass (Figures 2a and 3a) is the Rayleigh wave part of the Green function reconstructed from random noise correlations. Another signal with apparent velocity larger than 10 km/s (thin gray lines) is dominant in the 0.1–0.3 Hz bandpass (Figures 2a and 3a). This signal with very high apparent velocity is stronger during northern summer than winter. We hypothesize that those fast arrivals are *P* waves with steep incidence angle that are generated by very distant sources. During northern summer strong secondary microseisms are mostly expected to be generated within oceans in the southern hemisphere. For such sources, relatively short period surface waves are attenuated because of large propagating distances. This may explain why the noise correlations are dominated by near-zero time body wave arrivals. We test this hypothesis with a polarization analysis on cross-correlation signals. We demonstrate that the polarization of a plane wave recorded at two stations can be reliably estimated from the multicomponent cross correlations.

1.1.3. Polarization Analysis of a Plane Wave From Its Cross-Correlation Records: Method

[11] *Jurkevics* [1988] studied the polarization of different waves emitted by an earthquake using the covariance matrix of three-component record. He recovered the polarization angle and the azimuth from the eigenvectors of the covariance matrix. We demonstrate in the Appendix that the covariance matrix of the components at a single station (S_{CovSig}) is proportional to the covariance matrix of the cross-correlation signals (S_{CovCorr}) (equation (A10)) for a plane *P* wave propagating across a network of stations. Therefore, the eigenvectors are identical and the polarization analysis can be performed either on cross-correlation records at two stations or on three-component record at a single station.

[12] As suggested by *Jurkevics* [1988], the eigenvalues of the covariance matrix ($\lambda_1 > \lambda_2 > \lambda_3$) are used to compute the coefficient of rectilinearity *R*:

$$R = 1 - \frac{\lambda_2 + \lambda_3}{2\lambda_1}. \qquad (1)$$

which is equal to 1 for a rectilinear polarization. The eigenvector corresponding to the largest eigenvalue λ_1 gives the polarization angle and azimuth of the plane wave. The conversion from the polarization angle (φ) to the incidence angle (*I*) is obtained from the displacement equations for a reflected *P* wave at the free surface given by *Aki and Richards* [1980]. We use a ratio between *P* and *S* waves velocities of $V_P/V_S = \sqrt{3}$ for this conversion.

1.1.4. Polarization Analysis of Cross Correlations Computed With ETSE Data

[13] We use only station pairs with distance larger than 50 km to compute the covariance matrix of the three cross correlations ZE, ZN and ZZ. To prevent any influence of the Rayleigh wave (group velocity 3 km/s), we select time windows between −10 s and 10 s. Among the 127,490 cross-correlation signals available for 671 days and 190 station pairs, 23,449 signals are selected based on signal-to-noise (see section 1.1.1) and minimum distance criterion. This rather small percentage (18%) is due to time-variable data availability and quality. Daily records including earthquakes or glitches are removed from the database due to our water level amplitude filter.

[14] Using eigenvalues and eigenvectors of the covariance matrix, we compute the rectilinearity coefficient (equation (1)), the azimuth and the incidence angle for every interstation cross correlation. The rectilinearity coefficient over the whole experiment is 0.84 ± 0.12, which shows that the polarization of the studied wave is almost linear.

[15] Figure 4 shows particle motion for two daily cross correlations and two station pairs. Particle motion is shown in the horizontal plane (ZN as a function of ZE) and in the vertical propagation plane defined by the measured azimuth angle (ZZ as a function of ZH) where ZH is obtained by the rotation of the ZE and ZN components of the correlations using the azimuth angle measured from the polarization analysis. The rotation can be computed after the correlation because no nonlinear processing such as one-bit transform or spectral whitening has been applied to the data. The dashed lines in Figure 4 display the azimuth and incidence angle obtained from the covariance method. We observe that the displacement is stronger on the vertical component than on

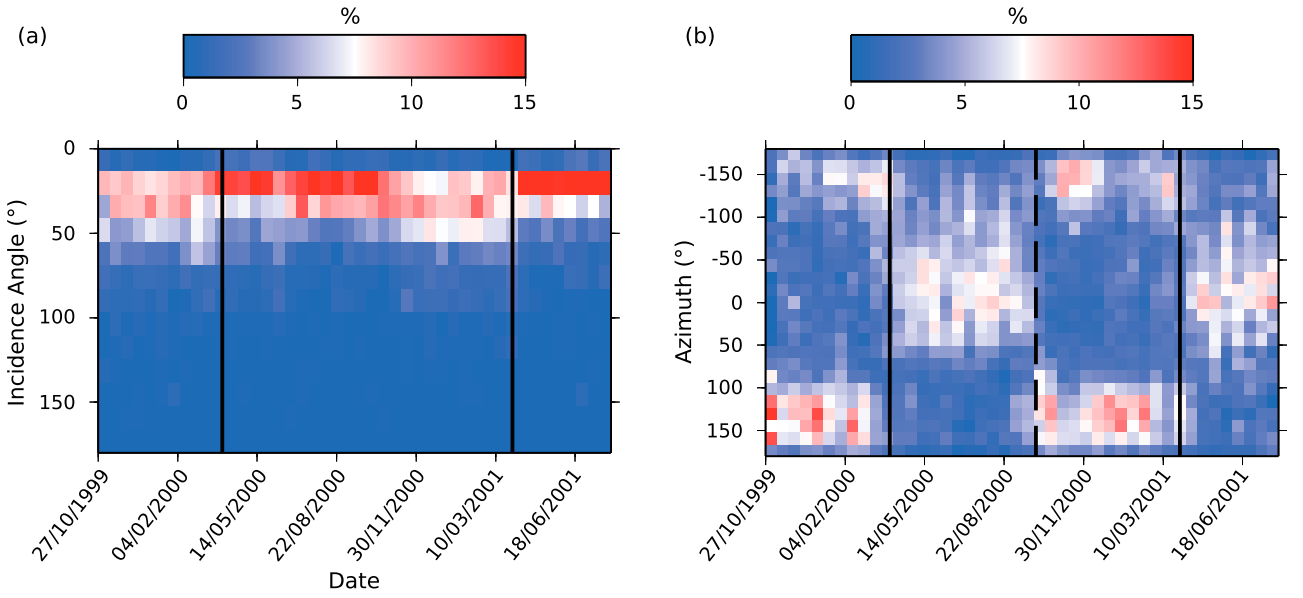


Figure 5. Probability of occurrence of a given value (a) of the incidence angle and (b) of the azimuth for 20 day time periods for all station pairs of the ETSE network. Continuous lines correspond to 1 April 2000 and 1 April 2001, and dashed line corresponds to 1 October 2000.

the horizontal ones suggesting that the signal observed on the cross correlations at near-zero times is composed of nearly vertically incident *P* waves.

[16] We then estimate the incidence angle and the azimuth of the body wave detected from correlations of ambient noise records and investigate their possible seasonal variations. Figure 5 shows the probability of occurrence of a given value of incidence angle (Figure 5a) and azimuth (Figure 5b) in a time period of 20 days evaluated from all daily records and station pairs. Figure 5a shows that we detect *P* waves with steep incidence angles during the whole experiment. It also documents a seasonal change of the incidence angle from an average of 15° in summer to 25° in winter, with a more accurate measurement of the incidence angle in the summer than in the winter (larger probability of occurrence). We observe the exact opposite in Figure 5b with better determined azimuths in winter than in summer, simply because the azimuth cannot be evaluated for an almost vertically incident *P* wave.

[17] The seasonal variation observed for the incidence angle is even clearer for the azimuth (Figure 5b). In summer, the average azimuth close to 0° shows that sources of the *P* waves are located south of the ETSE network. Winter noise sources are located northwest of the network as documented by azimuths close to 150°. Those observations are consistent with seasonal changes in the behavior of seismic noise sources [e.g., *Stehly et al.*, 2006; *Tanimoto et al.*, 2006]. The precise location of the sources of the *P* wave component of the noise will be investigated in section 2.

2. Locating Seismic Noise Sources With a Beam-Forming Analysis

[18] To determine regions that generate these body waves, we perform a beam-forming analysis of the noise cross correlations using the whole network as an array. We use only vertical components where the body waves are mostly detected. When studying a single component, we do not need to preserve the amplitude and, for efficiency, preprocess the continuous data with spectral whitening and one-bit normalization to improve the signal-to-noise ratio [*Larosse et al.*, 2004]. We analyze two frequency bands [0.05–0.1 Hz] and [0.1–0.3 Hz] corresponding to primary and secondary microseismic peaks, respectively.

2.1. Beam-Forming Analysis

[19] Our time shift beam-forming analysis consists of decomposing the body wave part of a wavefield recorded by a network into plane waves. If a plane wave defined by its slowness vector **S** reaches two stations A and B, the cross correlation of signals recorded at these stations will be shifted by

$$\Delta T_{AB}(\mathbf{S}) = \mathbf{S} \cdot \mathbf{AB} \tag{2}$$

where **AB** is the vector connecting A and B. We approximate the network to be flat by neglecting different station elevations and project the slowness vectors into the horizontal plane considering its south-north and west-east components S_N and S_E. For a given horizontal slowness vector $\mathbf{S} = (S_E, S_N)$, we time shift all interstation cross correlations following (2) and stack them to define the function C_{stack}:

$$C_{\text{stack}}(\mathbf{S}, t) = iFFT\left(\sum_{P \in PS} e^{2i\pi\omega\ \Delta T_P(\mathbf{S})} C_P(\omega)\right) \tag{3}$$

where *PS* represents the ensemble of pairs of stations, C_P is the Fourier Transform of the noise correlation for pair *P* and *iFFT* is the inverse Fourier transform. The characterization of the signal amplitude in the horizontal slowness domain is finally defined as:

$$A(\mathbf{S}) = \int_{-T}^{T} \Gamma(C_{\text{stack}}(\mathbf{S}, t))\ dt \tag{4}$$

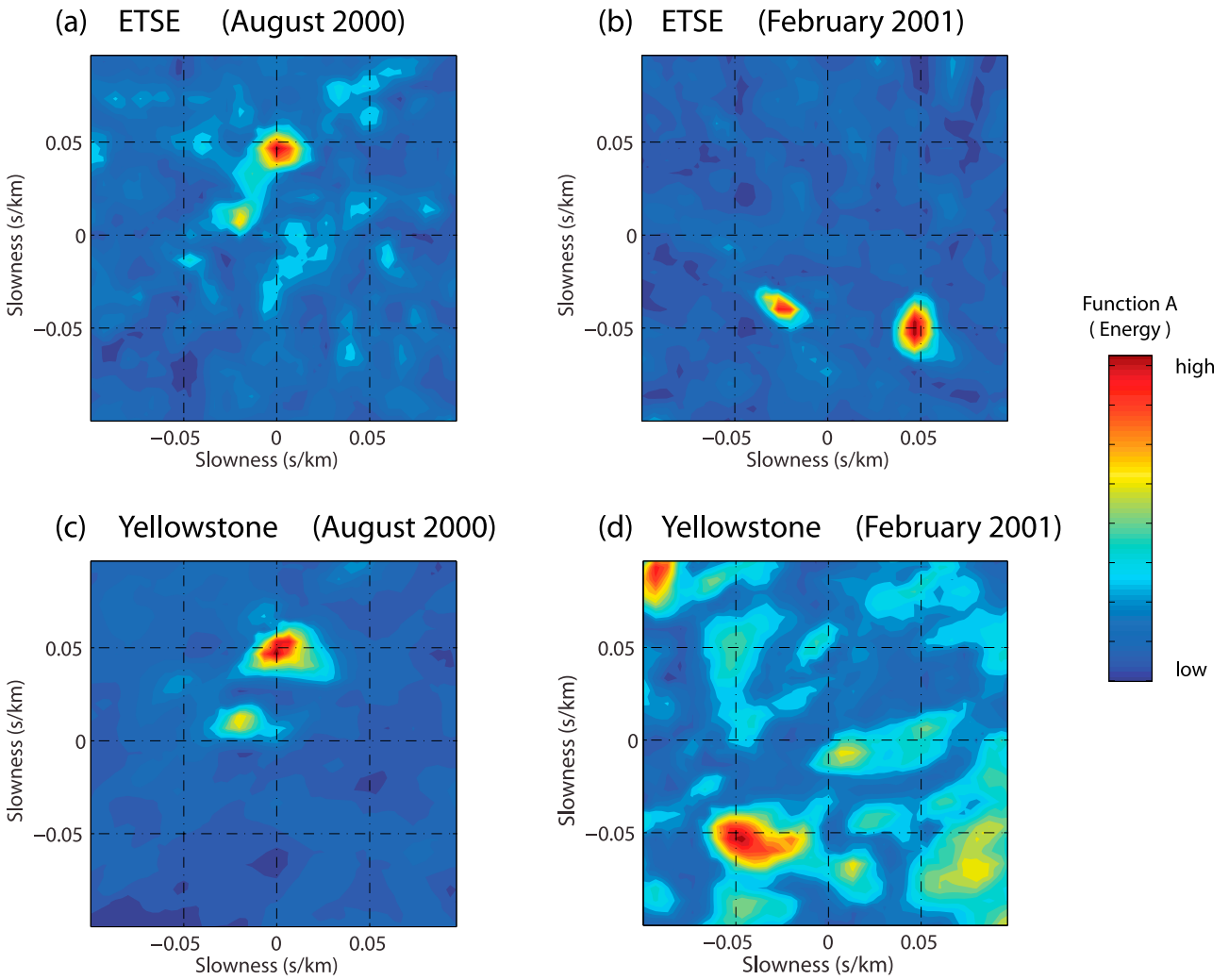


Figure 6. Beam-forming result of the Yellowstone and ETSE networks for August 2000 and February 2001 around the secondary microseismic peak (0.1–0.3 Hz).

where Γ [$f(t)$] returns the envelope of the function $f(t)$ using Hilbert transform. Integration limits [$-T$, T] are used to select the part of cross correlations centered at targeted slowness and we set T to be equal 15 s and 10 s for the primary and the secondary microseismic bands, respectively.

[20] Figure 6a shows results of the beam-forming analysis applied to 1 month cross correlations of the noise recorded by the ETSE network during August 2000 and filtered around the secondary microseismic peak (0.1–0.3 Hz). Energy distribution on the horizontal slowness plane is clearly not random and homogeneous. Two clear patches indicate that during this month most of body wave energy recorded by ETSE stations is arriving with rather fast apparent velocities (>20 km/s) and is coming from two preferential directions south and southeast of the network. A similar analysis made during February 2001 also shows two very localized patches of body wave energy with fast apparent velocities (Figure 6b). However, during this winter month the waves are coming from the north. These observation are in good agreement with seasonal variations of the location of sources of microseisms deduced from the polarization analysis and from previous studies [e.g., *Stehly et al.*, 2006].

[21] We then analyzed seismic noise recorded by a network operated in 2000–2001 in North America, i.e., by the Yellowstone PASSCAL experiment [*Fee and Dueker*, 2004]. Results of the beam-forming analysis for August 2000 and February 2001 shown in Figures 6c and 6d, respectively, are similar to observations made with the ETSE network. Localized noise sources are seen south of the network during the Northern hemisphere summer and north of the network during the winter.

2.2. Locating *P* Wave Noise Sources on the Earth's Surface

[22] In a next step, we project the results of the beam-forming analysis on the Earth's surface. Following the results of the polarization analysis of the near-zero time arrivals at cross correlations and their fast apparent velocities, we assume that they are mostly composed of teleseismic *P* waves. For a given slowness and back azimuth we can back project a seismic wave using a ray tracing in a

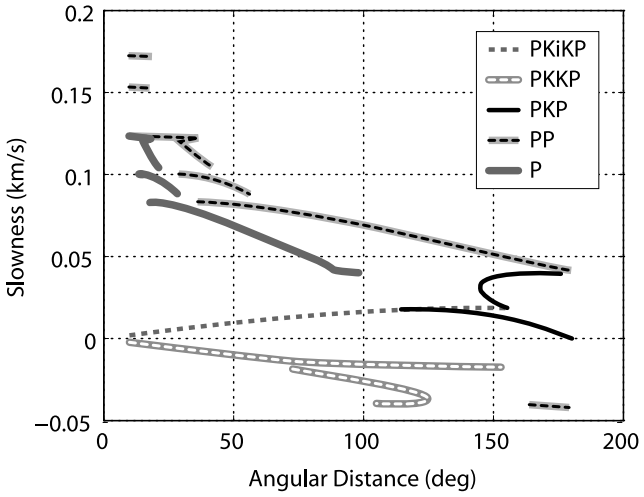


Figure 7. Variations of slowness (s/km) with respect to the angular distance (deg) for *P*, *PP*, *PKP*, *PKiKP*, and *PKIKP* phases.

spherically symmetric Earth's model. We suppose that diffracted and reflected phases are less energetic than direct and refracted waves and, therefore, the waves that we take into account are *P*, *PP*, *PKP*, *PKiKP*, and *PKIKP* waves and we use the IASPEI91 tables [*Kennett and Engdahl*, 1991] to relate the slowness with the source-receiver distance for all considered phases (Figure 7).

[23] For every point on the Earth's surface, we identify all phases that may propagate from this point to the network location and determine their horizontal slowness. Therefore, for each position we determine the "energy" of all the waves that are considered from the horizontal slowness plane. The energy is evaluated from the function *A* determined by the beam-forming analysis (equation (4)). Finally, we select the phase corresponding to the maximum value of the beam-forming map and attribute this amplitude to the projection at the considered geographical position. By repeating this procedure for all points on a 5° longitude × 2.5° latitude geographical grid we construct a map of what can be considered as probability density of noise sources during the considered period.

[24] This process is illustrated for three geographical locations shown with stars in Figure 8b and ETSE Network (triangle in Figure 8b). White lines are the great circles and their projections in the horizontal slowness plane in Figures 8b and 8a. For the location 1, the possible seismic phases are *PP*, *PKP* (branches ab and bc) and *PKiKP* (red line in Figure 8a) and the branch bc of the phase *PKP* corresponds to the strongest amplitude that is then selected for the projections. Similarly, for locations 2 and 3, possible phases are *PKiKP* and *P* or *PP*, respectively, and the latter correspond to stronger amplitudes and are used for the projection. The larger patch is projected as a *P* wave into the Indian ocean and as a *PP* wave into the southern Pacific. The smaller patch corresponds to a *PKP* wave originated in the vicinity of New Zealand.

[25] Maps of *P* wave noise source densities corresponding to beam-forming results from Figure 6 are shown in Figure 9. Some source areas such as the region south of Africa during August 2000 and Northern Atlantic south of Iceland during February 2001 are well illuminated by both networks. This suggests that strongest sources of *P* waves microseisms are

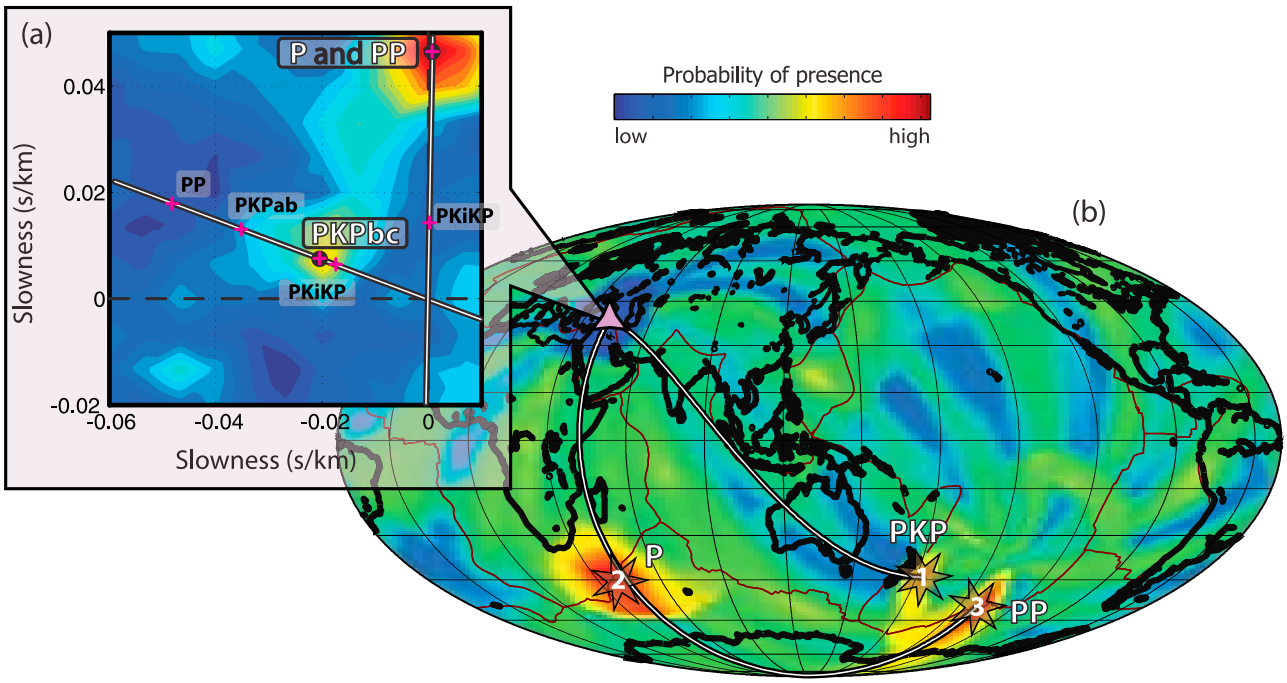


Figure 8. Illustration of projection of the beam-forming results on the Earth's surface (see text for explanations). (a) Results of the beam-forming analysis of noise cross correlations computed during August 2000 for the 0.1–0.3 Hz frequency band between stations of the Turkey network plotted as function of horizontal slowness. (b) Projection of these results on the Earth surface.

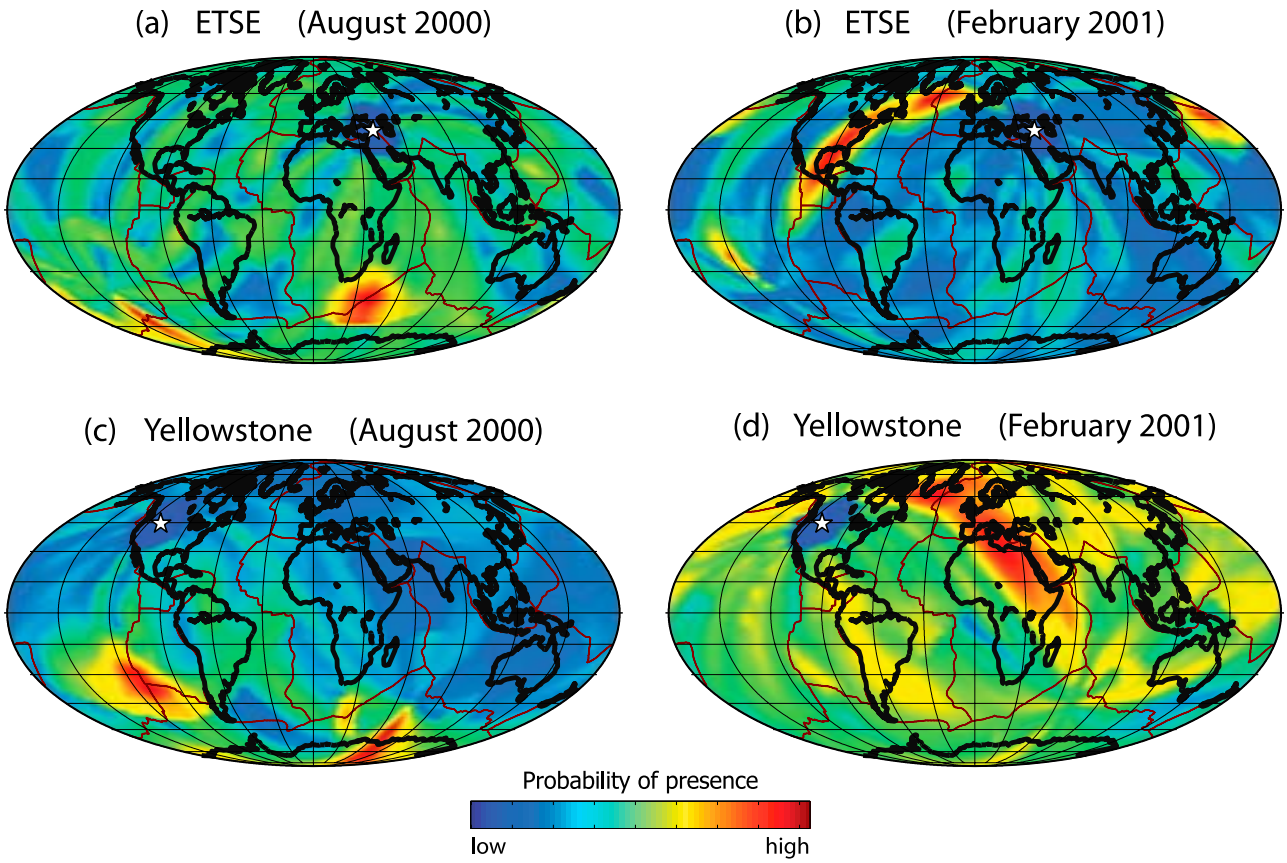


Figure 9. Projection results of the Yellowstone and ETSE networks for August 2000 and February 2001 around the secondary microseismic peak (0.1–0.3 Hz).

seen by multiple networks distributed around the world. Therefore, we decided to combine observations from different networks to improve the accuracy of the location of main sources of *P* wave microseisms. We used stations from three networks shown in Figure 1: 46 stations from Yellowstone park, 29 stations from ETSE, and 14 stations of the Kirgyz Seismic Network (KNET). We interpret the projection map obtained from every individual networks as a probability density and just multiply them to find the combined distribution.

[26] Location of *P* wave sources of the primary and secondary microseisms during different seasons are shown in Figures 10 and 11. For every map we used correlations of 1 month of data. In the secondary microseismic band, regions that generate *P* waves are well defined (Figure 10) and are mostly in deep oceans. Also, a clear seasonal migration can be observed with strongest sources located in the northern hemisphere during the northern hemisphere winter and in the southern hemisphere during the summer. In the primary microseismic band (Figure 11) we also observe a similar seasonal variation. However, uncertainties of the source location are much larger than in the secondary microseismic band. The reason for this is that the signal-to-noise ratio of the near-zero time arrival in cross correlations is much lower in the primary microseismic band than in the secondary microseismic band. Also, reliability of the array analysis degrades at longer wavelengths. Despite these large uncertainties, it is clearly seen in Figures 10 and 11 that in most cases, sources of primary microseisms do not coincide geographically with sources of secondary microseisms pointing to different physical mechanism of generation of these two microseismic peaks.

[27] The maps of Figure 11 are similar with the results of *Stehly et al.* [2006] in terms of seasonality. The location of noise sources based on the back propagation of Rayleigh waves cannot provide a resolution comparable to the one we achieved with body waves. Nevertheless, even with *P* waves, the uncertainties of location of sources of the primary microseism do not allow to clearly conclude unambiguously that they are located in deep parts of the ocean, in near-coastal regions, or both. While strongest identified source areas tend to extend to deep oceanic parts, they also cover coastal areas.

3. Discussion and Conclusion

[28] Results of our polarization and beam-forming analyses of the continuous noise records demonstrate that significant part of the microseismic noise is composed of *P* waves generated by distant sources. These sources show a clear seasonality in correlation with the seasonal migration of the strong oceanic storms between the southern and the northern hemisphere suggesting that the observed teleseismic *P* waves are generated by the interaction of waves produced by these storms with the seafloor. Location of *P* wave sources in the primary and in the secondary micro-

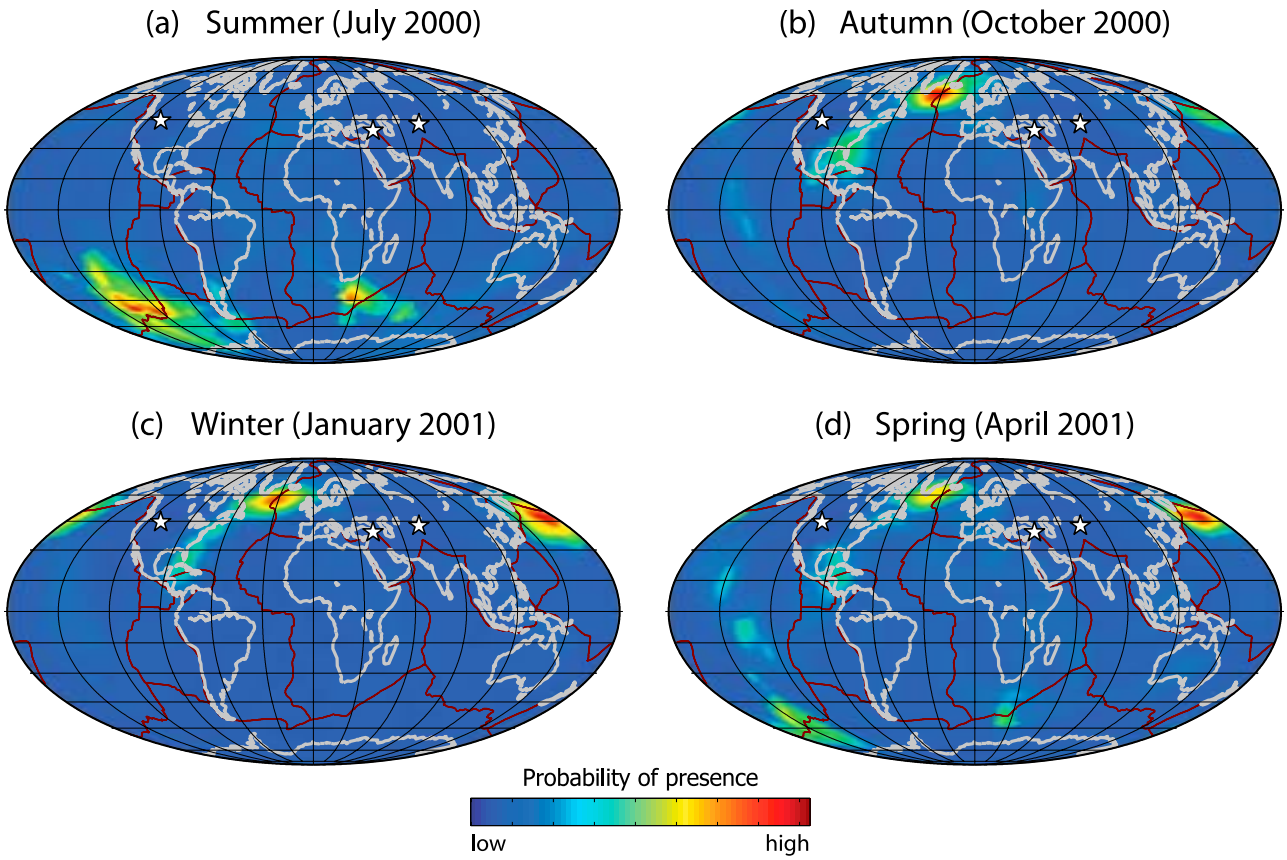


Figure 10. Seasonal variation of the location of *P* wave seismic noise sources in the secondary microseismic band (0.1–0.3 Hz).

seismic bands do not coincide with each other indicating that these two peaks are generated in different regions and possibly by different physical process. *P* waves are more easily identified in the secondary microseismic band than in the primary microseismic band. While we cannot exclude that this difference is related to the more efficient mechanism generating secondary microseismic *P* waves than primary ones, a simple explanation of this observation can be related to difference in wave propagation. Strong noise sources generate both body wave and surface waves. For the latter, their attenuation is much stronger at higher frequencies. Therefore, surface waves in the secondary microseismic peak propagate much less efficiently over very long distances than in the low-frequency primary microseismic band. As a consequence, for distant noise sources, the relative part of the body waves in the recorded seismic noise is relatively high in the secondary microseismic band while the primary microseismic band remains largely dominated by surface waves, making observation of *P* waves more difficult.

[29] Using array-based processing of the teleseismic *P* waves to locate regions generating strong microseisms has significant advantages relative to using surface waves [e.g., *Stehly et al.*, 2006]. The latter yields only a determination of their back azimuths at the array location while with body waves we can measure both back azimuths and slownesses that can be converted into distances. Therefore, we can locate the source regions more accurately with body waves than with surface waves.

[30] We can compare our maps of the source density in the secondary microseismic band (Figure 10) with results by *Gerstoft et al.* [2008], who applied beam-forming to the noise records of the Southern California seismic network. We find similar source locations in southern Pacific and Indian oceans during summer months and in northern Pacific and Atlantic ocean during winter months. Using three networks simultaneously allows us to image source regions with higher reliability. One of most important consequences of this improved reliability is that we clearly see that strongest sources of *P* wave microseisms are located in deep oceans far from coasts for the secondary microseism. Also, the observed source regions are significantly smaller than areas affected by significant wave heights. Overall our observations are consistent with the generation of microseisms by nonlinear interaction of ocean waves propagating in opposite directions that create a pressure distribution on the seafloor at twice the frequency of the interfering waves [*Longuet-Higgins*, 1950]. Following *Kedar et al.* [2008], this wave-wave interaction occurs in deep oceans and the geographical intensity of this interaction may be computed from oceanic wave action models. Moreover, the efficiency of the coupling between the interfering oceanic waves and the seafloor may depend on the depth of the water column, i.e., on the bathymetry. As a result, an efficient transfer of energy from oceanic to seismic waves occurs over geographically very limited and specific areas. It is in particular interesting to note that the source area near Iceland seen in Figure 10 during

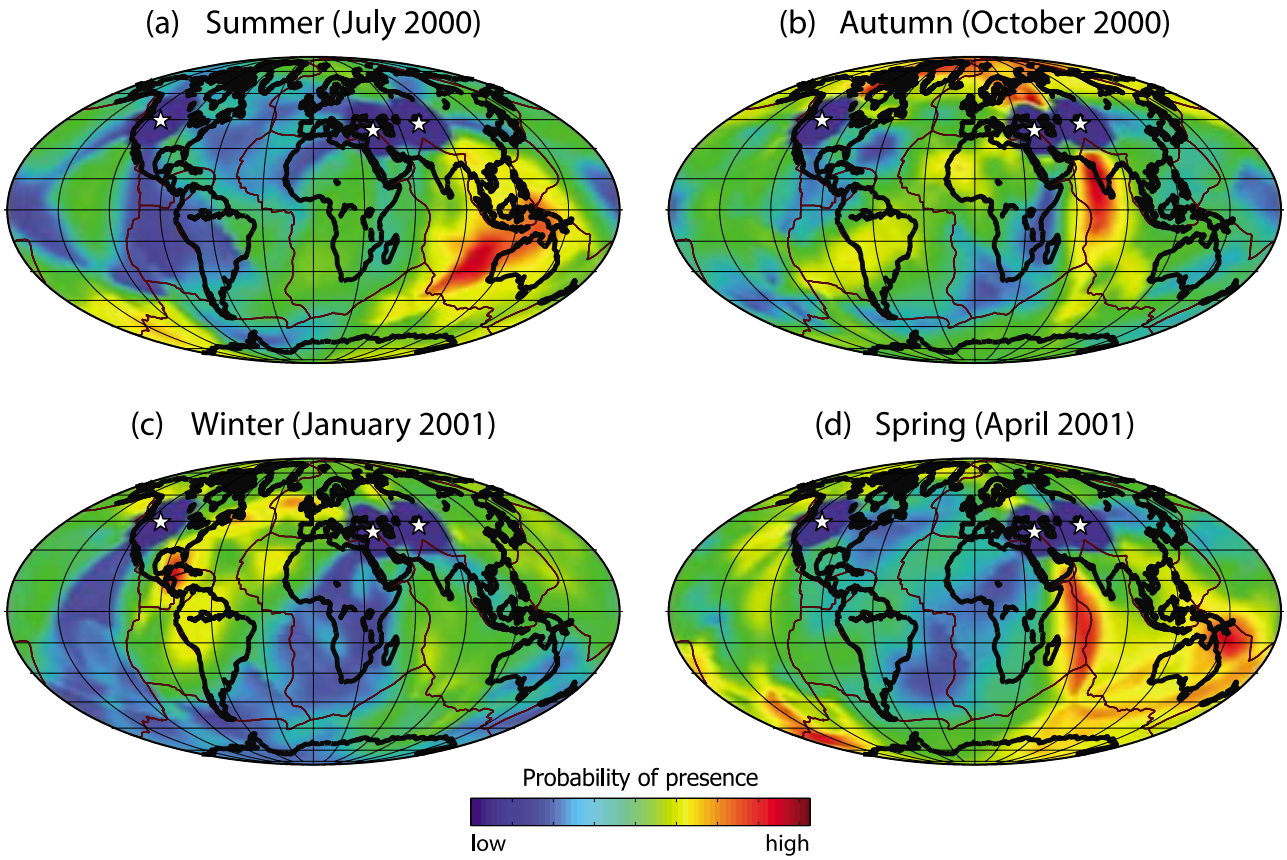


Figure 11. Seasonal variation of the localization of seismic noise in the primary microseismic bands (0.05–0.1 Hz).

October and January coincides with the strong source of Rayleigh wave microseisms computed by *Kedar et al.* [2008] based on Longuet-Higgins's theory and oceanic wave action models.

[31] These observations confirm that the source of secondary microseisms are not confined in the coastal areas as it is often accepted by seismologists. On average, the excitation of *P* waves by oceanic waves is stronger in the deep oceans. It does not mean, however, that there is no excitation along the coast, particularly when storms hit the shoreline.

[32] In the future, locating sources of *P* wave microseisms can be improved with using more networks better distributed over the globe. Observing and understanding these sources is important to validate predictive models of the seismic noise generation and distribution. These models, in turn, may help us to improve the accuracy of noise based seismic imaging and monitoring.

Appendix A: Wave Polarization Analysis From Cross Correlations

[33] We consider a plane wave with amplitude A, wave vector $\mathbf{k}$ and pulse shape $v(t)$. The azimuth (Az) is defined as the angle between the North and the projection of the wave vector in the horizontal plane. In the vertical plane, the incidence angle (I) is the angle between the vertical and the wave vector. Equation (A1) gives the general form of a three-component record of the signal that will be used for this demonstration:

$$\begin{aligned} S_N(t) &= A\sin(I)\cos(\mathrm{Az})v(t-T), \\ S_E(t) &= A\sin(I)\sin(\mathrm{Az})v(t-T), \\ S_Z(t) &= A\cos(I)v(t-T), \end{aligned} \tag{A1}$$

where T is the arrival time of the signal at the station.

[34] This plane wave is recorded at two different stations A and B at times $T = t_A$ and $T = t_B$. We compute three cross correlations between the vertical component of station A and the three components of station B. They are

$$\begin{aligned} ZN(t) &= A^2\cos(I)\sin(I)\cos(\mathrm{Az})V(t), \\ ZE(t) &= A^2\cos(I)\sin(I)\sin(\mathrm{Az})V(t), \\ ZZ(t) &= A^2\cos^2(I)V(t), \end{aligned} \tag{A2}$$

where

$$V(t) = \int_{-\infty}^{+\infty} v(\tau)\bar{v}[\tau - (t_B - t_A) - t]d\tau \tag{A3}$$

is the time correlation function and $\bar{v}(t)$ the complex conjugate of $v(t)$.

[35] The definition of the covariance between two signals (E and F) in the time window $[T_1, T_2]$ is given by

$$\mathrm{Cov}_{EF} = \int_{T_1}^{T_2} E(t)F(t)dt. \tag{A4}$$

For north and east component records of station A, we select a time window including the signal ($t_A \in [T_1, T_2]$) and we compute the covariance defined by equation (A4) to obtain

$$\mathrm{Cov}_{NE} = \int_{T_1}^{T_2} A^2 \sin^2(I)\cos(\mathrm{Az})\sin(\mathrm{Az})v(t-t_A)v(t-t_A)dt,$$
$$\mathrm{Cov}_{NE} = A^2 \sin^2(I)\cos(\mathrm{Az})\sin(\mathrm{Az})C, \tag{A5}$$

where $C = \int_{T_1}^{T_2} v(t-t_A)\, v\,(t-t_A)\, dt$ is a nonnull constant.

[36] We apply the same computation to all pairs of records at station A, and we obtain the covariance matrix of the three-component record:

$$S_{\mathrm{Cov}S_A} = CM, \tag{A6}$$

where

$$M = \begin{pmatrix} \cos^2(I) & \cos(I)\sin(I)\cos(\mathrm{Az}) & \cos(I)\sin(I)\sin(\mathrm{Az}) \\ \cos(I)\sin(I)\cos(\mathrm{Az}) & \sin^2(I)\cos^2(\mathrm{Az}) & \sin^2(I)\cos(\mathrm{Az})\sin(\mathrm{Az}) \\ \cos(I)\sin(I)\sin(\mathrm{Az}) & \sin^2(I)\cos(\mathrm{Az})\sin(\mathrm{Az}) & \sin^2(I)\sin^2(\mathrm{Az}) \end{pmatrix}. \tag{A7}$$

[37] We consider the definition of the covariance (equation (A4)) and the definition of the cross correlations between two stations (equation (A2)) to compute the covariance between ZE and ZN cross correlations. We select a time window $[T_1; T_2]$ of the correlation which includes the correlation of the initial signal:

$$\mathrm{Cov}_{Z_AE_B - Z_AN_B} = \int_{T_1}^{T_2} A^4 \cos^2(I)\sin^2(I)\cos(\mathrm{Az})\sin(\mathrm{Az})V(t)V(t)dt,$$
$$\mathrm{Cov}_{Z_AE_B - Z_AN_B} = A^4 \cos^2(I)\sin^2(I)\cos(\mathrm{Az})\sin(\mathrm{Az})C_{\mathrm{Corr}}, \tag{A8}$$

where $C_{\mathrm{Corr}} = \int_{T_1}^{T_2} V(t)\, V(t)\, dt$ is a nonnull constant.

[38] The covariance matrix for cross correlations is computed from equations (A2) and (A4):

$$S_{\mathrm{CovCorr_{AB}}} = A^4 \cos^2(I) C_{\mathrm{Corr}} M. \tag{A9}$$

$$S_{\mathrm{CovCorr}} = A^2 \cos^2(I) \frac{C_{\mathrm{Corr}}}{C} S_{\mathrm{Cov}S_A}. \tag{A10}$$

where $A^2 \cos^2(I) \frac{C_{\mathrm{Corr}}}{C}$ is a nonnull constant. From equation (A10) we conclude that in the case of a plane P wave, the covariance matrix for the three-component record at a single station and the covariance matrix for the cross correlations between two stations ($S_{\mathrm{Cov}S_A}$ and $S_{\mathrm{CovCorr_{AB}}}$, respectively) differ only by a scalar factor. Therefore, the eigenvectors of those matrix are the same which prove the polarization analysis can be performed either on cross correlation or on three-component records.

[39] **Acknowledgments.** The data of the "Eastern Turkey" and of the "Geodynamics of the Yellowstone Hot spot" seismic PASSCAL experiment as well as of the Kyrgyz Seismic Network used in this study were obtained through IRIS DMC. We thank Sharon Kedar and Frank Webb for helpful discussions and G. Moguilny for maintaining the Cohersis cluster. This work was supported by Agence Nationale de la Recherche (France) under contract ANR-06-CEXC-005 (COHERSIS) and by a FP7 ERC Advanced grant 227507 (WHISPER).

References

Aki, K., and P. Richards (1980), *Quantitative Seismology—Theory and Methods*, W. H. Freeman, New York.

Backus, M., J. Burg, D. Baldwin, and E. Bryan (1964), Wide-band extraction of mantle p waves from ambient noise, *Geophysics*, *29*, 672–692, doi:10.1190/1.1439404.

Brenguier, F., M. Campillo, C. Hadziioannou, N. M. Shapiro, R. M. Nadeau, and E. Larose (2008a), Postseismic relaxation along the San Andreas Fault at Parkfield from continuous seismological observations, *Science*, *321*, 1478, doi:10.1126/science.1160943.

Brenguier, F., N. Shapiro, M. Campillo, V. Ferrazzini, Z. Duputel, O. Coutant, and A. Nercessian (2008b), Towards forecasting volcanic eruptions using seismic noise, *Nat. Geosci.*, *1*, 126–130, doi:10.1038/ngeo104.

Bromirski, P. (2009), Earth vibrations, *Science*, *324*, 1026–1027, doi:10.1126/science.1171839.

Bromirski, P. D., and F. K. Duennebier (2002), The near-coastal microseism spectrum: Spatial and temporal wave climate relationships, *J. Geophys. Res.*, *107*(B8), 2166, doi:10.1029/2001JB000265.

Cessaro, R. K. (1994), Sources of primary and secondary microseisms, *Bull. Seismol. Soc. Am.*, *84*, 142–148.

Chevrot, S., M. Sylvander, S. Benahmed, C. Ponsolles, J. M. Lefvre, and D. Paradis (2007), Source locations of secondary microseisms in western Europe: Evidence for both coastal and pelagic sources, *J. Geophys. Res.*, *112*, B11301, doi:10.1029/2007JB005059.

Derode, A., E. Larose, M. Tanter, J. de Rosny, A. Tourin, M. Campillo, and M. Fink (2003), Recovering the Green's function from field-field correlations in an open scattering medium (L), *J. Acoust. Soc. Am.*, *113*, 2973–2976, doi:10.1121/1.1570436.

Essen, H.-H., F. Krger, T. Dahm, and I. Grevemeyer (2003), On the generation of secondary microseisms observed in northern and central Europe, *J. Geophys. Res.*, *108*(B10), 2506, doi:10.1029/2002JB002338.

Fee, D., and K. Dueker (2004), Mantle transition zone topography and structure beneath the Yellowstone hotspot, *Geophys. Res. Lett.*, *31*, L18603, doi:10.1029/2004GL020636.

Friedrich, A., F. Krüger, and K. Klinge (1998), Ocean-generated microseismic noise located with the Gräfenberg array, *J. Seismol.*, *2*, 47–64, doi:10.1023/A:1009788904007.

Gerstoft, P., and T. Tanimoto (2007), A year of microseisms in southern California, *Geophys. Res. Lett.*, *34*, L20304, doi:10.1029/2007GL031091.

Gerstoft, P., M. C. Fehler, and K. G. Sabra (2006), When Katrina hit California, *Geophys. Res. Lett.*, *33*, L17308, doi:10.1029/2006GL027270.

Gerstoft, P., P. M. Shearer, N. Harmon, and J. Zhang (2008), Global P, PP, and PKP wave microseisms observed from distant storms, *Geophys. Res. Lett.*, *35*, L23306, doi:10.1029/2008GL036111.

Gouédard, P., et al. (2008), Cross-correlation of random fields: mathematical approach and applications, *Geophys. Prospect.*, *56*, 375–393, doi:10.1111/j.1365-2478.2007.00684.x.

Iyer, H. M., and J. H. Healy (1972), Evidence for the existence of locally-generated body waves in the short-period noise at the large aperture seismic array, *Bull. Seismol. Soc. Am.*, *62*, 13–29.

Jurkevics, A. (1988), Polarization analysis of three-component array data, *Bull. Seismol. Soc. Am.*, *78*, 1725–1743.

Kedar, S., M. Longuet-Higgins, F. Webb, N. Graham, R. Clayton, and C. Jones (2008), The origin of deep ocean microseisms in the North Atlantic Ocean, *Proc. R. Soc. London, Ser. A*, *464*, 777–793, doi:10.1098/rspa.2007.0277.

Kennett, B. L. N., and E. R. Engdahl (1991), Traveltimes for global earthquake location and phase identification, *Geophys. J. Int.*, *105*, 429–465, doi:10.1111/j.1365-246X.1991.tb06724.x.

Koper, K. D., and B. de Foy (2008), Seasonal anisotropy in short-period seismic noise recorded in south Asia, *Bull. Seismol. Soc. Am.*, *98*, 3033–3045, doi:10.1785/0120080082.

Larosse, E., A. Derode, M. Campillo, and M. Fink (2004), Imaging from one-bit correlations of wideband diffuse fields, *Appl. Phys. Lett.*, *95*, 8393–8399, doi:10.1063/1.1739529.

Lobkis, O. I., and R. L. Weaver (2001), On the emergence of the Green's function in the correlations of a diffuse field, *J. Acoust. Soc. Am.*, *110*(6), 3011–3017, doi:10.1121/1.1417528.

Longuet-Higgins, M. S. (1950), A theory of the origin of microseisms, *Philos. Trans. R. Soc. London, Ser. A*, *243*, 1–35, doi:10.1098/rsta.1950.0012.

Rhie, J., and B. Romanowicz (2006), A study of the relation between ocean storms and the Earth's hum, *Geochem. Geophys. Geosyst.*, *7*, Q10004, doi:10.1029/2006GC001274.

Sabra, K., P. Gerstoft, P. Roux, W. Kuperman, and M. Fehler (2005), Surface wave tomography from seismic ambient noise in southern California, *J. Acoust. Soc. Am.*, *117*, 2431–2432.

Sánchez-Sesma, F. J., and M. Campillo (2006), Retrieval of the Green's function from cross correlation: The canonical elastic problem, *Bull. Seismol. Soc. Am.*, *96*, 1182–1191, doi:10.1785/0120050181.

Sandvol, E., N. Turkelli, E. Zor, R. Gok, T. Bekler, C. Gurbuz, D. Seber, and M. Barazangi (2003), Shear wave splitting in a young continent-continent collision: An example from eastern Turkey, *Geophys. Res. Lett.*, *30*(24), 8041, doi:10.1029/2003GL017390.

Schulte-Pelkum, V., P. S. Earle, and F. L. Vernon (2004), Strong directivity of ocean-generated seismic noise, *Geochem. Geophys. Geosyst.*, *5*, Q03004, doi:10.1029/2003GC000520.

Sens-Schönfelder, C., and U. Wegler (2006), Passive image interferometry and seasonal variations of seismic velocities at Merapi Volcano, Indonesia, *Geophys. Res. Lett.*, *33*, L21302, doi:10.1029/2006GL027797.

Seriff, A. J., C. J. Velzeboer, and R. J. Haase (1965), Possible P-wave observations in short-period seismic noise, *Geophysics*, *30*, 1187, doi:10.1190/1.1439709.

Shapiro, N. M., and M. Campillo (2004), Emergence of broadband Rayleigh waves from correlations of the ambient seismic noise, *Geophys. Res. Lett.*, *31*, L07614, doi:10.1029/2004GL019491.

Shapiro, N. M., M. Campillo, L. Stehly, and M. H. Ritzwoller (2005), High-resolution surface-wave tomography from ambient seismic noise, *Science*, *307*, 1615–1618, doi:10.1126/science.1108339.

Snieder, R. (2004), Extracting the Green's function from the correlation of coda waves: A derivation based on stationary phase, *Phys. Rev. E*, *69*(4), 046610, doi:10.1103/PhysRevE.69.046610.

Stehly, L., M. Campillo, and N. M. Shapiro (2006), A study of the seismic noise from its long-range correlation properties, *J. Geophys. Res.*, *111*, B10306, doi:10.1029/2005JB004237.

Stehly, L., B. Fry, M. Campillo, N. M. Shapiro, J. Guilbert, L. Boschi, and D. Giardini (2009), Tomography of the Alpine region from observations of seismic ambient noise, *Geophys. J. Int.*, *178*, 338–350, doi:10.1111/j.1365-246X.2009.04132.x.

Tanimoto, T., S. Ishimaru, and C. Alvizuri (2006), Seasonality in particle motion of microseisms, *Geophys. J. Int.*, *166*, 253–266, doi:10.1111/j.1365-246X.2006.02931.x.

Toksöz, M. N., and R. T. Lacoss (1968), Microseisms: Mode structure and sources, *Science*, *159*, 872–873, doi:10.1126/science.159.3817.872.

Yang, Y., and M. H. Ritzwoller (2008), Characteristics of ambient seismic noise as a source for surface wave tomography, *Geochem. Geophys. Geosyst.*, *9*, Q02008, doi:10.1029/2007GC001814.

Yang, Y., M. H. Ritzwoller, A. L. Levshin, and N. M. Shapiro (2007), Ambient noise Rayleigh wave tomography across Europe, *Geophys. J. Int.*, *168*, 259–274, doi:10.1111/j.1365-246X.2006.03203.x.

M. Campillo, F. Hubans, and A. Paul, Laboratoire de Géophysique Interne et Tectonophysique, Maison des Géosciences, BP 53, F-38041 Grenoble CEDEX 9, France. (Michel.Campillo@ujf-grenoble.fr; fabien.hubans@obs.ujf-grenoble.fr; Anne.Paul@obs.ujf-grenoble.fr)

M. Landès and N. M. Shapiro, Équipe de Sismologie, Institut de Physique du Globe de Paris, 4 place Jussieu, F-75252 Paris, France. (landes@ipgp.jussieu.fr; nshapiro@ipgp.jussieu.fr)